

Circuit Quantum Electrodynamics Architecture for Gate-Defined Quantum Dots in Silicon

X. Mi,¹ J. V. Cady,^{1, a)} D. M. Zajac,¹ J. Stehlik,^{1, b)} L. F. Edge,² and J. R. Petta¹

¹⁾Department of Physics, Princeton University, Princeton, New Jersey 08544, USA

²⁾HRL Laboratories LLC, 3011 Malibu Canyon Road, Malibu, California 90265, USA

We demonstrate a hybrid device architecture where the charge states in a double quantum dot (DQD) formed in a Si/SiGe heterostructure are read out using an on-chip superconducting microwave cavity. A quality factor $Q = 5,400$ is achieved by selectively etching away regions of the quantum well and by reducing photon losses through low-pass filtering of the gate bias lines. Homodyne measurements of the cavity transmission reveal DQD charge stability diagrams. These measurements indicate that electrons trapped in a Si DQD can be effectively coupled to microwave photons, potentially enabling coherent electron-photon interactions in silicon.

PACS numbers: 03.67.Lx, 73.21.La, 42.50.Pq, 85.35.Gv

Silicon is an emerging material system for spin-based quantum computing due to record long quantum coherence times.^{1,2} Spin states of electrons in semiconductor quantum dots (QDs), long recognized to be highly promising candidates for the storage of quantum information,³ have limited coherence times in traditional host materials such as GaAs due to fluctuations of the nuclear spin bath.^{4,5} In silicon, owing to the zero nuclear spin carried by the naturally abundant isotope ²⁸Si, hyperfine induced dephasing of electron spins is strongly reduced.⁶ In contrast with III/V semiconductor compounds, silicon has weak spin-orbit coupling and can be isotopically enriched to the level of 800 ppm ²⁹Si for further enhancement of spin coherence times.⁷

Quantum devices based on Si can potentially be scaled to larger system sizes using well-developed semiconductor fabrication processes. Recent advances include the demonstration of two-qubit logic gates⁸ and the fabrication of a one-dimensional chain of nine QDs that was measured using three proximal charge detectors.⁹ Moreover, the long coherence times that have been reported in Si pave the way for long range coupling of spin states using superconducting cavities in the circuit quantum electrodynamics (cQED) architecture.^{10,11}

The field of cQED experimentally realizes on-chip interactions between a two-level system (the qubit) and photons confined within a superconducting microwave cavity.¹² Such cavities typically have frequencies between 1 and 10 GHz, which match the transition frequencies of many nanofabricated quantum devices and are therefore suitable mediators of non-local qubit interactions, providing a means for long range scaling of solid state qubits. In cQED systems with superconducting qubits, cavity photons are also widely used for dispersive state readout,

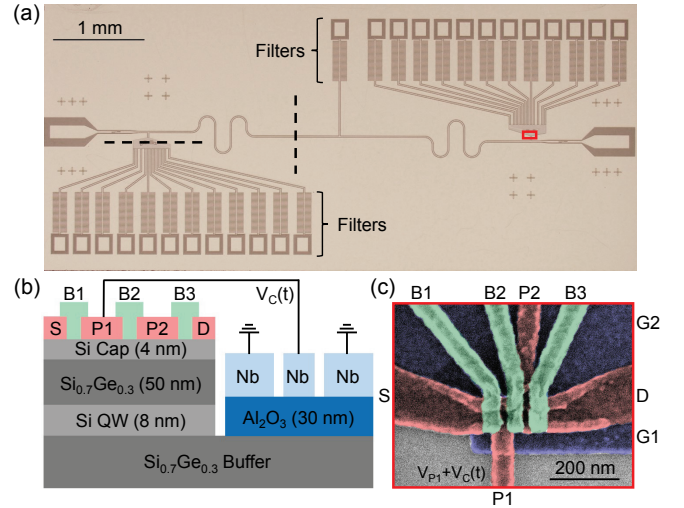


FIG. 1. (Color Online). (a) Optical image of a silicon hybrid cQED device. A Si DQD is placed at each voltage anti-node of the cavity. LC filters reduce leakage of cavity photons through dc biasing lines. (b) A cross-section (not to scale) taken along the horizontal dashed line in (a) shows the overlapping Al gates that define the DQD and the Si/SiGe heterostructure layers. To minimize internal losses the quantum well is removed in areas beneath the cavity center pin [cross-section through the vertical dashed line in (a)]. (c) False-color scanning electron microscope image of a DQD.

as the significant electric dipole moments of these devices result in large phase shifts in the cavity response.^{13,14} In semiconductor systems, hybrid cQED devices have been successfully implemented using GaAs,^{15,16} InAs,¹⁷ carbon nanotube,¹⁸ and graphene QDs.¹⁹ There are several proposals pertaining to the coupling of Si spin qubits to cavities,^{20,21} as well as the demonstration of a high kinetic inductance cavity, fabricated with the intention of coupling to Si quantum dots.²²

In this Letter, we present a hybrid cQED device architecture that couples a silicon DQD to a superconducting cavity. The device has three key components: a half-

^{a)}Present Address: Department of Physics, University of California Santa Barbara, Santa Barbara, California 93106, USA

^{b)}Present Address: IBM T.J. Watson Research Center, Yorktown Heights, New York 10598, USA

wavelength co-planar waveguide (CPW) cavity, two gate-defined DQDs, and low-pass LC filters that serve to reduce microwave losses through the dc bias lines that are used to tune DQD. This paper is organized as follows. We describe the device layout and fabrication process, the LC filter design considerations, and then demonstrate readout of DQD charge states using the cavity.

The devices are fabricated on Si/SiGe heterostructures grown by chemical vapor deposition.^{23,24} A $3\text{ }\mu\text{m}$ thick linearly graded $\text{Si}_{1-x}\text{Ge}_x$ relaxed buffer substrate is grown on top of a Si wafer (resistivity $> 5000\text{ }\Omega\text{-cm}$). The buffer is chemically and mechanically polished before the growth of a $170 - 375\text{ nm}$ thick $\text{Si}_{0.7}\text{Ge}_{0.3}$ layer, an 8 nm thick Si quantum well (QW), a $50 - 60\text{ nm}$ thick $\text{Si}_{0.7}\text{Ge}_{0.3}$ spacer and a $2 - 4\text{ nm}$ thick Si cap. Wafers grown under similar conditions have maximum mobilities $\mu = 650,000\text{ cm}^2/\text{Vs}$ and can support electron densities up to $n = 8 \times 10^{11}/\text{cm}^2$.

The cavity fabrication process is designed to achieve two major goals: protection of the Si QW from the reactive ions used to etch the Nb cavity and the reduction of internal photon losses introduced by two-level system (TLS) defects at the heterostructure interfaces. The Si QW in the area under the cavity center pin is first removed through a 70 nm deep reactive ion etch to minimize the internal photon loss. A 30 nm thick Al_2O_3 film, which serves as an etch stop for cavity fabrication, is then grown over the entire substrate using atomic layer deposition. Next, a 50 nm thick Nb film is deposited via dc sputtering. The cavity and filter patterns, shown in Fig. 1(a), are defined with a second reactive ion etch step using a SF_6/Ar plasma. A hydrofluoric acid etch then removes the Al_2O_3 film in the area where the DQD is to be defined. The resulting cross-sections of the device are schematically illustrated in Fig. 1(b).

Accumulation-mode DQDs are defined using an overlapping gate architecture.⁹ A scanning electron microscope image of the DQD is shown in Fig. 1(c). For the measurements presented here, electrons are only accumulated in one of the DQDs and the other DQD does not contribute to the cavity response. The first Al layer, shaded in purple, consists of two large gates G1 and G2 that selectively screen the electrostatic potentials of the upper Al layers and form a quasi-one-dimensional transport channel. The second Al layer, shaded in pink, consists of two plunger gates P1 and P2 that are used to tune the chemical potentials of the DQD, as well as source (S) and drain (D) accumulation gates. P1 is connected to the cavity center pin and capacitively couples the DQD to the time-dependent voltage $V_C(t)$ of the cavity. A dc tap is placed at the voltage node of the cavity and used to dc bias gate P1. The third Al layer, shaded light green, consists of three tunnel barrier gates. Gate B2 tunes the interdot tunnel coupling (t_c), gate B1 tunes the dot 1–source reservoir coupling, while gate B3 tunes the dot 2–drain reservoir coupling.

In comparison with superconducting qubit cQED devices, which generally support $Q > 50,000$,²⁵ hybrid QD-

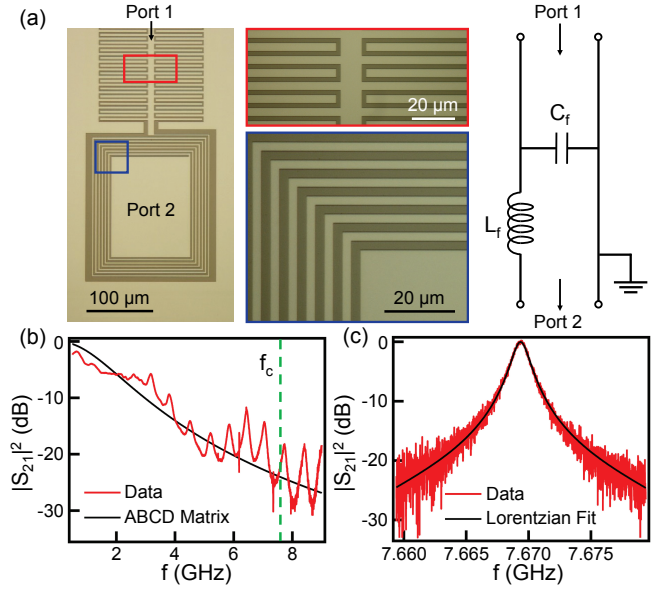


FIG. 2. (Color Online). (a) Left: Optical image of a compact LC filter, showing the spiral inductor and a portion of the capacitor. Middle: Zoomed-in view of the capacitor (red outline)/inductor (blue outline). Right: Circuit model for the LC filter. (b) Measured LC filter transmission $|S_{21}|^2$ (red) and ABCD matrix predictions (black). (c) Cavity transmission, $|S_{21}|^2$, measured with the DQD in Coulomb blockade. The black line is a fit to a Lorentzian with $Q = 5400$.

cQED systems generally have $Q = 1,000 - 3,000$.^{15–17,19} To coherently couple QD qubits to cavity photons, higher quality factors are needed. Measurements on previously reported device designs¹⁷ show significant microwave leakage through the dc bias lines leading to the DQD, which we attribute to the capacitive coupling between the cavity and each of the dc bias lines. The bias lines therefore become leakage pathways that inadvertently lower the Q . To minimize microwave leakage, we insert an LC filter in each dc bias line. An LC filter is also used to dc bias the cavity, in contrast to previous devices that used a spiral inductor on the dc tap and no filter along gate bias lines.¹⁷ Figure 2(a) shows the image of a single filter, which consists of a long interdigitated capacitor with $C_f \approx 1\text{ pF}$ and a spiral inductor with $L_f \approx 13\text{ nH}$. The overall dimensions of a filter are $700\text{ }\mu\text{m}$ by $200\text{ }\mu\text{m}$.

To evaluate the attenuation of the filter, we measure its transmission $|S_{21}|^2$ at a temperature $T = 1.5\text{ K}$. The data, shown in Fig. 2(b), display a clear roll-off with frequency f . Oscillations with a frequency spacing of $\sim 500\text{ MHz}$ are also seen throughout the data range. The oscillations may be due to reflections at the wire bonds connecting the filter to the circuit board, parasitic modes introduced by discontinuities in the ground plane, and parasitic capacitances/inductances that result from the relatively large size of the filter components. On average, 20 dB of attenuation is obtained around the cavity center frequency $f_c = 7.67\text{ GHz}$ [Fig. 2(c)].

For comparison, $|S_{21}|^2$, as calculated using the ABCD

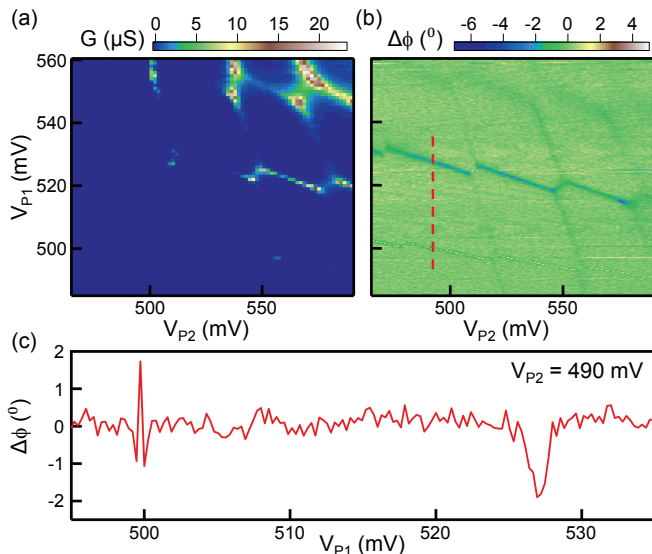


FIG. 3. (Color Online). (a) Conductance of the DQD, G , measured as a function of the voltages V_{P1} and V_{P2} on plunger gates P1 and P2. (b) Cavity phase response, $\Delta\phi$, measured over the same gate voltage range as (a). (c) $\Delta\phi$ plotted as a function of V_{P1} , with V_{P2} fixed at 490 mV [dashed line in (b)].

matrix approach, is plotted in Fig. 2(b).²⁶ The theory predicts a filter attenuation of 24 dB at $f = 7.67$ GHz. With the exception of the oscillations in the data, the overall transmission through the filter is in good agreement with theory. The undesired oscillations may be suppressed by using air-bridges to better connect distinct regions of the cavity ground plane, and improved circuit board designs to minimize the impedance of the wirebonds.²⁷

The incorporation of LC filters into the cavity design results in a significant increase in the cavity quality factor (cQED devices of the same DQD design without LC filters have $Q < 1,000$). Figure 2(c) shows the normalized cavity transmission $|S_{21}|^2$ as a function of f with the DQD configured in Coulomb blockade at $T = 10$ mK. The input power $P_{\text{in}} \approx -130$ dBm corresponds to an intra-cavity photon number $n \approx 3$. A fit to a Lorentzian function yields $Q = 5,400$, corresponding to a total photon loss rate $\kappa/2\pi = f_c/Q = 1.4$ MHz. Using the Sonnet EM simulation program, we estimate the cavity input and output coupling rates to be $\kappa_{\text{in}}/2\pi = \kappa_{\text{out}}/2\pi = 0.4$ MHz. The remaining loss rate of 0.6 MHz may be attributed to a combination of internal loss due to the dielectric layers under the cavity and remnant microwave leakage through the LC filters. The internal loss may be reduced by etching away Al_2O_3 and $\text{Si}_{0.7}\text{Ge}_{0.3}$ in the gap between the cavity center pin and the ground plane where the electric field intensity is large. Microwave leakage can be further suppressed through improved filter designs such as multi-pole LC filters and band-stop filters.²⁸

We next form a DQD at $T = 10$ mK using the overlapping Al gate architecture [Fig. 1(c)]. Figure 3(a) shows the DQD conductance, G , which is measured as a function of the plunger gate voltages V_{P1} and V_{P2} . A low frequency ac lock-in technique is used with an excitation voltage $V_{\text{SD}} = 10 \mu\text{V}$ and the electron temperature $T_e = 110$ mK.²⁹ A DQD charge stability diagram is clearly visible in these data, as evidenced by the triple points in the conductance. Cotunneling lines are also visible in the upper right quadrant of Fig. 3(a) due to relatively large dot-lead tunneling rates.

The high quality factor cavity allows for sensitive charge state detection, enabling a complementary measurement of the DQD stability diagram. We probe the cavity transmission using a homodyne measurement technique. The input port of the cavity is driven at a fixed frequency $f = f_c$ and power $P_{\text{in}} = -121$ dBm ($n \approx 20$), while the signal exiting the cavity is amplified and demodulated to yield the amplitude and phase response. We plot the cavity phase response $\Delta\phi$ as a function of V_{P1} and V_{P2} in Fig. 3(b). The DQD charge stability diagram is revealed in the cavity phase response, with the boundaries of charge stability islands delineated by non-zero values of $\Delta\phi$. Here charge dynamics in the DQD result in dispersive shifts in the cavity center frequency, inducing a phase shift in the transmitted signal.^{15,30,31} Dot 1 charge transitions generally have a larger visibility in the data since plunger gate P1 is directly connected to the cavity.

In contrast with quantum point contact based charge detectors, which probe the local electric field, cavity-based readout approaches are sensitive to the charge susceptibility of the DQD.^{15,30,31} Changes in the cavity transmission are most pronounced when the energy of a cavity photon hf_c is comparable to $\hbar\Gamma$, where Γ is the tunnel rate associated with a given charge transition.^{30,31} As such, cavity-based charge sensing can be used to map out a DQD charge stability diagram and extract information about the tunneling rate at each charge transition.

For example, the data in Fig. 3(b) show that the phase shift associated with dot 1 charge transitions is a function of the gate voltage V_{P1} . Around $V_{P1} = 550$ mV, the charge transition is weak and broad. Here the tunnel rate between dot 1 and its adjacent lead, Γ_{P1} , is much greater than f_c and the cavity is mostly decoupled from dot 1 transitions. The large tunnel rates in this region are also evident in Fig. 3(a), where broad cotunneling lines are visible. Around $V_{P1} = 520$ mV, the dot 1 charge transition is pronounced and characterized by a large negative phase shift $\Delta\phi < 0$. Here $\Gamma_{P1} > f_c$ and the coupling between the cavity and the electron in dot 1 is largely capacitive. Near $V_{P1} = 500$ mV, dot 1 transitions result in a positive phase shift $\Delta\phi > 0$. In this regime $\Gamma_{P1} < f_c$ and the coupling becomes predominantly inductive due to the lagging of electric current behind the fast variations of the cavity field.³⁰ Figure 3(c) shows $\Delta\phi$ as a function of V_{P1} , obtained from a cut through the data in Fig. 3(b) at $V_{P2} = 490$ mV.

Lastly, we estimate the capacitive and inductive loads of the DQD by approximating the cavity as a parallel *LCR* oscillator.³² The DQD may be modeled as an additional circuit element in parallel with the *LCR* oscillator.³⁰ In the capacitive regime, the DQD adds an amount C_q to the overall capacitance C of the cavity, reducing its resonance frequency $f_c = \frac{1}{2\pi} \sqrt{\frac{1}{LC}}$. Based on the observed phase response of $\Delta\phi = -2^\circ$, we estimate $C_q \approx 5$ aF, comparable to previously reported values.^{30,33} In the inductive regime, the inductance L_q of the DQD is in parallel with the inductance of the cavity L , reducing the total inductance and therefore increasing the resonance frequency. From the observed phase response $\Delta\phi = 1.8^\circ$, we estimate $L_q \approx 100$ μ H. This value is consistent with the large impedance of the DQD.^{30,31}

In conclusion, we have demonstrated readout of a Si/SiGe DQD that is embedded in a superconducting cavity. A quality factor $Q = 5,400$ is achieved by minimizing photon losses through the use of compact, on-chip *LC* filters. The DQD stability diagram is visible in measurements of the phase response of the cavity and analysis of the phase response at dot-lead charge transitions yields qualitative information on the relative magnitude of the dot-lead tunneling rate and cavity frequency. Looking ahead, this hybrid Si/SiGe QD cQED system could be used for the spectroscopy of low-lying valley states in Si,³⁴ demonstrations of strong coupling,¹² and explorations of the resonant exchange regime of triple quantum dots.^{20,21}

ACKNOWLEDGMENTS

We acknowledge valuable discussions with T. M. Hazard, Y.-Y. Liu, and S. Putz and thank J. Kerckhoff for suggesting the *LC* filters. Research was sponsored by ARO grant W911NF-15-1-0149 and the National Science Foundation (DMR-1409556 and DMR-1420541). The views and conclusions contained in this Letter are those of the authors and should not be interpreted as representing the official policies, either expressly or implied, of the United States Department of Defense or the U.S. Government. Devices were fabricated in the Princeton University Quantum Device Nanofabrication Laboratory.

- ¹A. M. Tyryshkin, S. Tojo, J. J. L. Morton, H. Riemann, N. V. Abrosimov, P. Becker, H.-J. Pohl, T. Schenkel, M. L. W. Thewalt, K. M. Itoh, and S. A. Lyon, *Nat. Mater.* **11**, 143 (2012).
- ²K. Saeedi, S. Simmons, J. Z. Salvail, P. Dluhy, H. Riemann, N. V. Abrosimov, P. Becker, H.-J. Pohl, J. J. L. Morton, and M. L. W. Thewalt, *Science* **342**, 830 (2013).
- ³D. Loss and D. P. DiVincenzo, *Phys. Rev. A* **57**, 120 (1998).
- ⁴J. R. Petta, A. C. Johnson, J. M. Taylor, E. A. Laird, A. Yacoby, M. D. Lukin, C. M. Marcus, M. P. Hanson, and A. C. Gossard, *Science* **309**, 2180 (2005).
- ⁵R. Hanson, L. P. Kouwenhoven, J. R. Petta, S. Tarucha, and L. M. K. Vandersypen, *Rev. Mod. Phys.* **79**, 1217 (2007).
- ⁶M. A. Eriksson, M. Friesen, S. N. Coppersmith, R. Joynt, L. J. Klein, K. Slinker, C. Tahan, P. M. Mooney, J. O. Chu, and S. Koester, *Quantum Inf. Proc.* **3**, 133 (2004).

- ⁷J.-Y. Li, C.-T. Huang, L. P. Rokhinson, and J. C. Sturm, *Appl. Phys. Lett.* **103**, 162105 (2013).
- ⁸M. Veldhorst, C. H. Yang, J. C. C. Hwang, W. Huang, J. P. Dehollain, J. T. Muhonen, S. Simmons, A. Laucht, F. E. Hudson, K. M. Itoh, A. Morello, and A. S. Dzurak, *Nature* **526**, 410 (2015).
- ⁹D. M. Zajac, T. M. Hazard, X. Mi, E. Nielsen, and J. R. Petta, e-print arXiv:1607.07025.
- ¹⁰M. A. Sillanpaa, J. I. Park, and R. W. Simmonds, *Nature* **449**, 438 (2007).
- ¹¹J. Majer, J. M. Chow, J. M. Gambetta, J. Koch, B. R. Johnson, J. A. Schreier, L. Frunzio, D. I. Schuster, A. A. Houck, A. Wallraff, A. Blais, M. H. Devoret, S. M. Girvin, and R. J. Schoelkopf, *Nature* **449**, 443 (2007).
- ¹²A. Wallraff, D. I. Schuster, A. Blais, L. Frunzio, R.-S. Huang, J. Majer, S. Kumar, S. M. Girvin, and R. J. Schoelkopf, *Nature* **431**, 162 (2004).
- ¹³D. Riste, M. Dukalski, C. A. Watson, G. de Lange, M. J. Tiggelman, Y. M. Blanter, K. W. Lehnert, R. N. Schouten, and L. DiCarlo, *Nature* **502**, 350 (2013).
- ¹⁴R. Vijay, D. H. Slichter, and I. Siddiqi, *Phys. Rev. Lett.* **106**, 110502 (2011).
- ¹⁵T. Frey, P. J. Leek, M. Beck, A. Blais, T. Ihn, K. Ensslin, and A. Wallraff, *Phys. Rev. Lett.* **108**, 046807 (2012).
- ¹⁶H. Toida, T. Nakajima, and S. Komiyama, *Phys. Rev. Lett.* **110**, 066802 (2013).
- ¹⁷K. D. Petersson, L. W. McFaul, M. D. Schroer, M. Jung, J. M. Taylor, A. A. Houck, and J. R. Petta, *Nature* **490**, 380 (2012).
- ¹⁸J. J. Viennot, M. C. Dartailh, A. Cottet, and T. Kontos, *Science* **349**, 408 (2015).
- ¹⁹G.-W. Deng, D. Wei, J. R. Johansson, M.-L. Zhang, S.-X. Li, H.-O. Li, G. Cao, M. Xiao, T. Tu, G.-C. Guo, H.-W. Jiang, F. Nori, and G.-P. Guo, *Phys. Rev. Lett.* **115**, 126804 (2015).
- ²⁰J. M. Taylor, V. Srinivasa, and J. Medford, *Phys. Rev. Lett.* **111**, 050502 (2013).
- ²¹M. Russ and G. Burkard, *Phys. Rev. B* **92**, 205412 (2015).
- ²²N. Samkharadze, A. Bruno, P. Scarlino, G. Zheng, D. P. DiVincenzo, L. DiCarlo, and L. M. K. Vandersypen, *Phys. Rev. Appl.* **5**, 044004 (2016).
- ²³C. Payette, K. Wang, P. J. Koppinen, Y. Dovzhenko, J. C. Sturm, and J. R. Petta, *Appl. Phys. Lett.* **100**, 043508 (2012).
- ²⁴X. Mi, T. M. Hazard, C. Payette, K. Wang, D. M. Zajac, J. V. Cady, and J. R. Petta, *Phys. Rev. B* **92**, 035304 (2015).
- ²⁵C. M. Quintana, A. Megrant, Z. Chen, A. Dunsworth, B. Chiaro, R. Barends, B. Campbell, Y. Chen, I.-C. Hoi, E. Jeffrey, J. Kelly, J. Y. Mutus, P. J. J. O'Malley, C. Neill, P. Roushan, D. Sank, A. Vainsencher, J. Wenner, T. C. White, A. N. Cleland, and J. M. Martinis, *Appl. Phys. Lett.* **105**, 062601 (2014).
- ²⁶D. Pozar, *Microwave Engineering, 4th Edition* (Wiley, 2011).
- ²⁷Z. J. Chen, A. Megrant, J. Kelly, R. Barends, J. Bochmann, Y. Chen, B. Chiaro, A. Dunsworth, E. Jeffrey, J. Y. Mutus, P. J. J. O'Malley, C. Neill, P. Roushan, D. Sank, A. Vainsencher, J. Wenner, T. C. White, A. N. Cleland, and J. M. Martinis, *Appl. Phys. Lett.* **104**, 052602 (2014).
- ²⁸N. T. Bronn, Y. Liu, J. B. Hertzberg, A. D. Crcoles, A. A. Houck, J. M. Gambetta, and J. M. Chow, *Appl. Phys. Lett.* **107**, 172601 (2015).
- ²⁹C. W. J. Beenakker, *Phys. Rev. B* **44**, 1646 (1991).
- ³⁰T. Frey, P. J. Leek, M. Beck, J. Faist, A. Wallraff, K. Ensslin, T. Ihn, and M. Büttiker, *Phys. Rev. B* **86**, 115303 (2012).
- ³¹L. E. Bruhat, J. J. Viennot, M. C. Dartailh, M. M. Desjardins, T. Kontos, and A. Cottet, *Phys. Rev. X* **6**, 021014 (2016).
- ³²M. Goppl, A. Fragner, M. Baur, R. Bianchetti, S. Filipp, J. M. Fink, P. J. Leek, G. Puebla, L. Steffen, and A. Wallraff, *J. Appl. Phys.* **104**, 113904 (2008).
- ³³J. I. Colless, A. C. Mahoney, J. M. Hornibrook, A. C. Doherty, H. Lu, A. C. Gossard, and D. J. Reilly, *Phys. Rev. Lett.* **110**, 046805 (2013).
- ³⁴G. Burkard and J. R. Petta, e-print arXiv:1607.08801.